PHOTONICS Research

Directional emission in X-cut lithium niobate microresonators without chaos dynamics

Ang Gao,[1,2,†] Chen Yang,[1,†] Likun Chen,[2,†] Ru Zhang,[1] Qiang Luo,[1] Wei Wang,[2] Qitao Cao,[2] Zhenzhong Hao,[1] Fang Bo,[1,3] Guoquan Zhang,[1,4] and Jingjun Xu[1,5]

[1]MOE Key Laboratory of Weak-Light Nonlinear Photonics, TEDA Institute of Applied Physics and School of Physics, Nankai University, Tianjin 300457, China
[2]State Key Laboratory for Artificial Microstructure and Mesoscopic Physics, School of Physics, Peking University, Beijing 100871, China
[3]e-mail: bofang@nankai.edu.cn
[4]e-mail: zhanggq@nankai.edu.cn
[5]e-mail: jjxu@nankai.edu.cn

We systematically investigate the field distribution of the transverse electric modes in X-cut lithium niobate disks as an example of circular microcavities with anisotropic refractive index. A conserved quantity is discovered, which indicates the absence of chaos that generally exists in deformed microcavities and leads to a nontrivial directional emission. The emission directionality was theoretically investigated and experimentally verified by exciting high-order modes of an X-cut lithium niobate microresonator assisted with second harmonics. The field distribution analysis can enrich the knowledge in designing photonic devices that need precise control of field distribution, such as phase matching in nonlinear processes. Furthermore, the discovered emission phenomenon is momentous in enhancing and controlling communications between on-chip photonic devices.   © 2022 Chinese Laser Press

https://doi.org/10.1364/PRJ.447488

1. INTRODUCTION

Whispering-gallery-mode (WGM) microcavities are well known for enhancing light intensity in a tremendously small spatial region [1,2], showing excellent performance in photonics applications such as lasing [3], sensing [4], and frequency combs [5,6]. Meanwhile, from the perspective of optical materials, thin-film crystals represented by lithium niobate on insulator (LNOI) which features superior $\chi^{(2)}$ nonlinearity in optics [7,8] and nice accessibility in integration, dominate the construction of chip-scale photonic devices such as optical parametric oscillators [9–12] and electro-optic modulators [13–16]. To fully use the $\chi^{(2)}$ property, LNOI with crystal axis that lies in the plane of a thin LN layer, also known as X-cut LNOI, is introduced to construct photonic components, which paves the way for a better combination of LN and WGM microcavities, leading to the advent of a series of novel devices. Specifically, X-cut LN circular microcavities have been intensively studied for their effectiveness in elevating the efficiency of electro-optic modulation as well as broadening the bandwidth of the phase-matching window in the parametric process [17–19].

However, such systems are not isotropic due to the strong birefringence in the material. In X-cut birefringent microcavities, the inconstant propagation direction of TE polarization light in a circular resonator breaks the rotational uniformity in refractive index, and just like other asymmetric resonators, optical fields inside it will deviate from a symmetric one. They may manifest various phenomena such as chaos [20], controllable directional emission [21], and broadband coupling [22]. Although a previous work by Park *et al.* has introduced transformed optics to analyze birefringent microcavities and foreseen directional emission in X-cut birefringent microdisks [23], a thorough research into the modes in such a system is yet to be presented, and the emission of these modes has not been tested by experiment.

In this paper, we propose and demonstrate an accurate identification of TE resonant modes in the geometrically symmetric optical microresonators made of X-cut uniaxial crystal, which yields strong mode localization and conspicuous directional emission patterns in simulation and experiment. The modified ray dynamics introduced into the analysis proves that this system supports WGMs with azimuthally modulated field distribution governed by a conserved quantity. For experimental verification, X-cut LN microdisks are fabricated, and the directional emission patterns are collected at the visible band with the assistance of a nonlinear process, in which high-order TE modes are excited as the second-harmonic signal. This rigorous depiction of optical modes can contribute to the accurate design of the phase-matching technique in the nonlinear process

and significant enhancement of the coupling between different optical devices [24,25].

2. THEORY

Considering the hardness of analytical solution in wave dynamics, ray dynamics is applied to predict the behavior of light in X-cut LN microdisks. Ray dynamics simply treats light as billiards in a closed region with perfect reflecting walls [26]. It successfully demonstrates the diverse mode properties, such as chaos, island mode, and directional emission, in geometrically uniform resonators. Here, we applied this method to circular disk resonators with an anisotropic refractive index, as shown in Fig. 1(a). Generally, the incidence and reflection directions do not coincide in a circular X-cut LN resonator with a rotationally symmetric shape due to the birefringence [27]. The reflection angle χ/α for the wave vector/the Poynting vector for given incident angles can be solved at each reflection position φ following the momentum and energy conservation:

$$n_w(\theta_i) \sin \chi_i = n_w(\theta_{i+1}) \sin \chi_i', \qquad (1)$$

$$\tan \xi_i = \frac{n_o^2}{n_e^2} \tan \theta_i, \qquad (2)$$

where θ/ξ stands for the angle between the wave vector/ Poynting vector and the crystal axis, i indicates the reflection times, and $n_w(\theta)$ is the refractive index of the wave vector. For TE modes where electric field mainly lies in the disk plane,

$$n_w(\theta) = \frac{n_o n_e}{\sqrt{n_e^2 \cos^2 \theta + n_o^2 \sin^2 \theta}}, \qquad (3)$$

n_o and n_e are the ordinary and extraordinary refractive indices of LN, respectively. Considering the geometrical relations, the angles follow

$$\varphi_i = \pi - \varphi_{i-1} + 2\xi_{i-1}, \qquad \chi_i = \theta_{i-1} - \varphi_i. \qquad (4)$$

Consequently, the reflection angle χ for the wave vector that is the characteristic variable to identify the traces of light in the ray model [20] can be solved at each given φ. The set of real space ray trajectories can be manifested in the phase space customarily called the Poincaré surface of section (PSOS). The PSOS diagram for a typical X-cut LN disk resonator is shown in Fig. 1(b), where the ray trajectories for the modes with radial quantum numbers q of 1, 3, 5, 7, 9, and 11 are demonstrated from top to bottom in black lines. It is seen that the phase space is composed of separated winding curves corresponding to the WGMs with different radial quantum numbers q. Moreover, the critical line for the total internal reflection defined by $n_w(\theta) \sin \chi = 1$ is indicated as the lowest line colored in green in Fig. 1(b). It sets up a limitation in the largest q for the resonant modes because the orbits intersecting or lying below the critical line cannot satisfy total internal reflection and thus experience severe loss due to refraction.

To verify the validity of the ray dynamics, the real space field of TE WGMs obtained by using 2D COMSOL simulation was projected into the phase space according to Husimi function [28–32]. The results for WGMs with $q = 3, 11$ are drawn in Fig. 1(b) as the pseudo-color images in blue and orange, respectively, showing a good agreement in two aspects below.
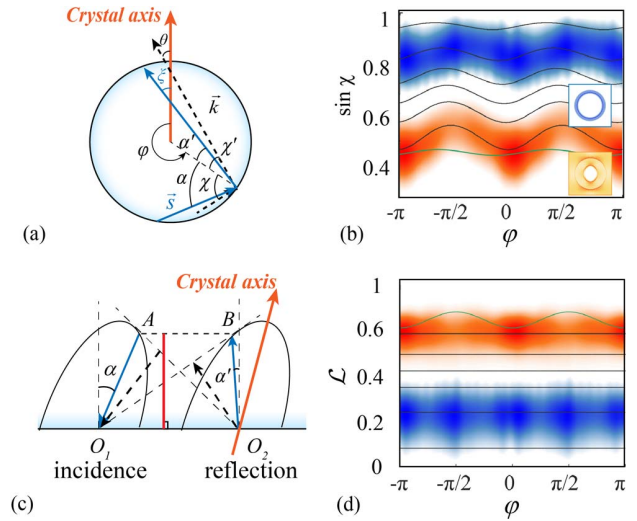

Fig. 1. (a) Illustration of ray dynamics in X-cut uniaxial disks. Blue, black, and orange arrows denote the wave vector, Poynting vector, and crystal axis, respectively. (b) PSOS and emerging Husimi function of modes, in which the field distribution was acquired from the simulation with size parameter $kR = 40$. The defused areas colored in blue and orange represent the electric-field distribution of modes with $q = 3$ and $q = 11$, respectively. Insets: real-space profile of the corresponding modes. (c) A close-up of the reflection point in (a). The incident beam and reflected beam with a time interval Δt are shown. The conserved quantity is depicted in the Huygens's wave propagation diagram, where the red line denotes $c\sqrt{\mathcal{L}}/(\sqrt{n_o n_e}\Delta t)$. (d) Phase space spanned by position φ and the conserved quantity $\mathcal{L}$.

First, in PSOS in Fig. 1(b), the orbits calculated from the ray model coincide with the ribbons from field simulation. Second, when q increases, both lines and ribbons move downward in PSOS and demonstrate stronger vibration.

Most importantly, we found that the algebraic relation of ray dynamics leads to a conserved quantity:

$$\mathcal{L} = \frac{n_o n_e \sin^2(\varphi - \xi)}{n_e^2 \sin^2 \xi + n_o^2 \cos^2 \xi} = \frac{n_o n_e \cos^2 \alpha}{n_r^2(\varphi, \alpha)}, \qquad (5)$$

where n_r is the refractive index for the Poynting vector. The physical meaning of $\mathcal{L}$ can be found out from Fig. 1(c), where the red line represents $c\sqrt{\mathcal{L}}/(\sqrt{n_o n_e}\Delta t)$, implying the energy conservation in the normal direction of the interface. To be specific, the normal component of energy flow of the incident beam (proportional to $\cos \alpha/n_r$) is equal to that of the reflected beam. This is because the resonator is conservative both in ray analysis and field simulation, when the tunneling caused by the curvature of the boundary is neglected. Meanwhile, due to the circular shape of the resonator, the reflected angle is preserved as the incident angle in the next reflection, making the value of $\mathcal{L}$ preserved in the next reflection.

An additional conserved quantity in dynamics proves the integrability of ray orbits in the phase space and distinguishes X-cut LN resonators from most asymmetric resonators. The latter usually manifest chaos and directional emission in propagation dynamics due to the instability in the solution of ray model equations after multiple iterations. According to Eq. (5), curves in Fig. 1(b) can be transformed into lines of constant $\mathcal{L}$,

as illustrated in Fig. 1(d). Notice that $\mathcal{L}$ and $\sin\chi$ are inversely correlated; therefore, modes with higher q lie higher in the phase diagram in Fig. 1(d).

In Fig. 1(d), the total reflection condition is manifested as a wavy line, which prevents light lying higher in this phase diagram from being totally reflected. Thus, WGMs located on high $\mathcal{L}$ orbits exhibit directional emission at the azimuthal position $\varphi = 0$ and $\varphi = \pi$, when the total reflection condition was unsatisfied. Such a directional emission is different from the geometrically uniform resonators in the view of physical origin. Typically, direction emission in geometrically asymmetric resonators results from the violation of the total internal reflection condition over regions at the boundary due to chaotic dynamics. However, the directional emission in X-cut LN microdisks is contributed by the field perturbation caused by the distribution of refractive index and evanescent tunneling in the integrable dynamics regime.

From the view of wave optics, the conservation is not strict as shown by the Husimi distribution of the COMSOL-calculated mode field of the WGMs with q equal to 3 and 11 in Figs. 1(b) and 1(d). However, the existence of the conserved quantity $\mathcal{L}$ and the directional emission is demonstrated as well. In this theoretical framework, the scale of the resonator influences the far-field property by altering the diffusion of Husimi distribution in the PSOS. A microcavity with a scale that is too small to satisfy the ray approximation will suffer an extra escape of light at the boundary, which increases the uniform far-field background and spoils the unidirectionality of mode emission.

3. SIMULATION

From the previous deduction, we can learn that the directional emission is mainly affected by the intersection between $\mathcal{L}$ and the total reflection line as well as diffusion of the Husimi distribution of the mode. The former is influenced by the ratio between n_o and n_e according to Eq. (5). The latter one is related to the scale of the resonator. Theoretically, the directional emission is caused by the inhomogeneous leakage of whispering gallery modes over regions of the microdisk. As long as the radial quantum number (q) of a mode is large enough, an intersection between the Husimi distribution of that mode and the total reflection curve in the PSOS will exist inevitably, so all modes that diffuse significantly across the critical curve are emissive. However, the following discussions are targeted on the resonant emissive modes with lowest $\mathcal{L}$, since they are confined tightly and possess merits such as higher Q factor and narrower emission angle benefits from their little contact with the total reflection curve. Accordingly, we investigated and optimized the emission, and the results are shown in Fig. 2. The simulation is done with 2D COMSOL. The obtained eigenmodes are supposed to be standing wave modes, which can be decomposed into clockwise (CW) and counter-clockwise (CCW) components since only modes that propagate in either of the two directions can be excited in experiments.

Practically, the birefringence-induced anisotropic field distribution is modulated by n_o and n_e, whose ratio is a wavelength-dependent variable due to material dispersion. Therefore, we set kR as a constant 40.5 and investigate the
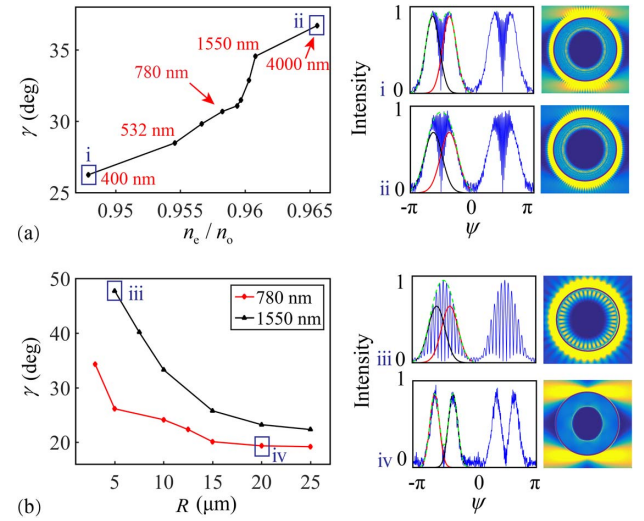

Fig. 2. Emission directionality regulated by (a) the ratio between n_e/n_o and (b) the radius of the microcavity, where the far-field angle is defined as γ. (a) Emission property of modes in X-cut LN microdisks with $kR = 40.5$ at 400 nm, 532 nm, 633 nm, 780 nm, 980 nm, 1064 nm, 1310 nm, 1550 nm, 2100 nm, and 4000 nm, respectively. (b) Emission property in the band of 780 nm and 1550 nm. The far-field angle varies slowly when $R \geq 20\ \mu m$. Right: a selection of four far-field emission intensity and near-field patterns related to the data points in the left panel, denoted by (i)–(iv). Black, red, and blue curves represent the CW, CCW, and standing wave modes.

directional emission at the wavelengths of a series of widely used commercialized lasers with n_o and n_e given by the Sellmeier equation for LN crystal [33]. The dependence of the smallest dispersion angle γ on the ratio between n_o and n_e is shown in Fig. 2(a), from which it is clearly seen that the emission directionality is in essence regulated by the ratio of n_o and n_e. This phenomenon is comparable to that in an elliptic resonator with uniform refractive index by coordinate transformation [23]. Second, we examine how the scale of microcavity affects the emission pattern by checking the emission in both 780 nm and 1550 nm bands in cavities with various radii. The results are shown in Fig. 2(b). The far-field distribution and mode profile of emissive modes under typical circumstances are plotted in the right panel both in Figs. 2(a) and 2(b), where the huge difference between emission patterns can be observed clearly while changing the configuration of the microdisk. Along with the increase in radius, the emission angle of modes decreases and tends to vary slowly when the scale of the resonator is considerably large ($\geq 20\ \mu m$) due to the gradual coincidence between the ray model and light field distribution. In comparison, the far-field angle at 780 nm band is smaller than that at the 1550 nm band in a given cavity because the former has a more significant contrast between the wavelength and the radius of the resonator.

4. EXPERIMENT

In order to verify the predicted field distribution and directional emission, LN microdisks were fabricated from an X-cut LN wafer bonded onto an LN substrate with a deposited silica

buffer layer. First, by using lithography and reactive ion etching, we formed LN cylinders on silica film. Then chemo-mechanical polishing was employed to refine the surface and periphery of LN microdisks to raise the Q factor, leaving a faint gradual thinning at the periphery. Lastly, hydrogen fluoride etching was used to remove silica to form a free-standing LN disk resonator. As a result, a microdisk that has a 20 μm radius, a 550 nm thickness, and a smooth sidewall with a 70° wedge angle was finally obtained. Furthermore, the microdisk is specially designed in geometry to obtain 780 nm band directional emission in a relatively small angle based on simulation results in Fig. 2(b).

The experimental setup shown in Fig. 3(a) was utilized to visualize the mode patterns with obvious directionality. Theoretically, high-order whispering gallery modes in the 1550 nm band can be emitted directionally. However, to demonstrate directional emission clearly, a 1550 nm band pump was launched into the fundamental TE mode of the disk to excite the mode in the 780 nm band with relatively large radial quantum numbers as well as strong directional emissions via the second-harmonic generation (SHG) process instead of directly exciting. Light emitted from the tunable diode laser was coupled into the resonator with a tapered fiber, and the transmission spectrum was recorded while sweeping the frequency of the pump. Figure 3(a) shows the scanning electron image of a fabricated LN microdisk. The loaded Q of the X-cut LN disk is as high as 1.2×10^6 indicated by the transmission spectrum shown in Fig. 3(d). With the selection rule of polarization for the components of the $\chi^{(2)}$ matrix, the second-harmonic modes are naturally TE polarized when the pump has a TE polarization [18]. Figure 4(a) shows the broadband transmission spectrum around 1550 nm, where modes were identified by comparing the experimental resonant frequencies with the calculated ones considering the geometric parameters of the LN disk. To simplify the demanding simulation, we used a 2D model to calculate the mode distribution in the section view of the microdisk. The refractive index of the TE mode in
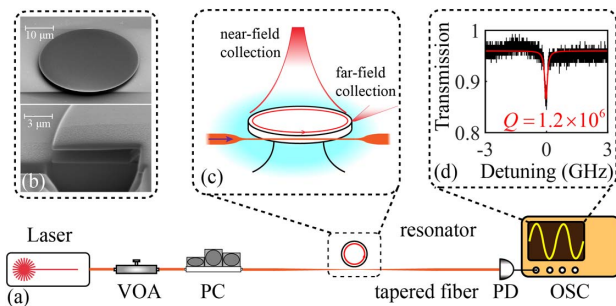

Fig. 4. (a) Transmission spectrum from 1535 nm to 1570 nm with the mode characterization in simulation. Insets: field patterns of the pump and SHG mode, respectively. Simulations are done by setting the refractive index of material as the average one of TE modes over regions. (b) Near-field pattern from the top viewer. Inset: far-field intensity from the side viewer. Red and green curves denote the experimental and simulation result, respectively. (c) Near-field intensity at the periphery of the resonator. The demonstrated data are extracted from the $R = 20.1$ μm circle near the disk boundary shown in (b).

Fig. 3. Experimental setup and characterization of the X-cut LNOI microdisks. (a) Setup to study the pattern of high-order modes excited by second-harmonic generation. VOA, variable optical attenuator; PC, polarization controller; PD, photodetector; OSC, oscilloscope. (b) Scanning electron microscopy images of the LN microresonator for geometric parameter measurements of LN disks. (c) A close-up of the light collection system for both near-field and far-field measurement. (d) Q factor measurement of a typical whispering gallery mode of the resonator.
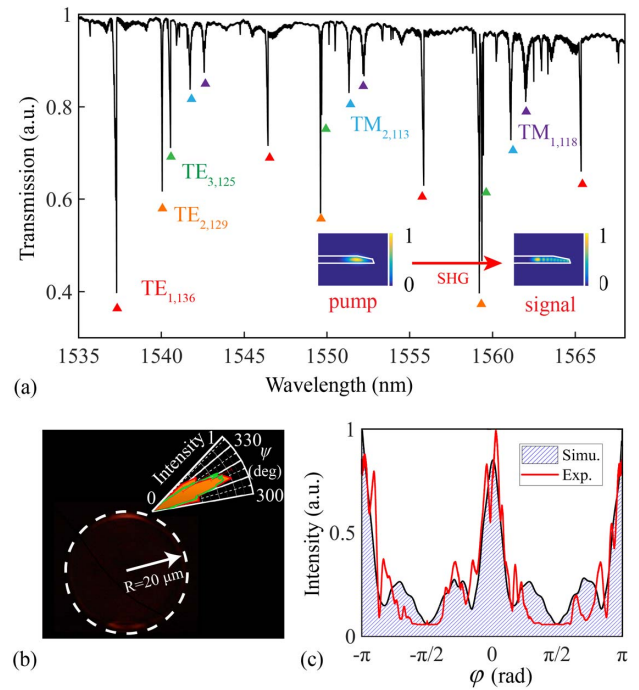
simulation was set as the average refractive index over regions in the anisotropic microdisk [18], which is also known as the arithmetic-geometric mean of n_o and n_e. For typical mode families including TE_1, TE_2, TE_3, and TM_1, differences in resonant wavelengths obtained from experiment and simulation are less than 0.02 nm, indicating the correctness of our mode identification. In experiments, the $TE_{1,133}$ mode at 1565.48 nm served as the pump, and generated the $TE_{9,265}$ SHG mode at 782.7 nm as a result.

The high Q factor and quasi-phase-matching condition promise efficient SHG [10], making the visualization of the field pattern possible even when the pump power was only 5.35 mW. The field pattern in the visible band is obtained in the vertical and horizontal directions [see Fig. 3(b)], respectively. The near-field pattern is indicated by the top view image shown in Fig. 4(b). Meanwhile, the far-field pattern was measured by the side view microscopy subtending a 2°36′ collection angle and the result with a 5° collection step is shown in the inset of Fig. 4(b), where the green line represents the simulation result while the red line depicts experimental data. A major emission peak with a far-field angle of 23° is observed, which is consistent with the simulation result marked in Fig. 4(b). Moreover, in order to make a comparison with the simulation result and clarify the anisotropic distribution of field, we extracted the near-field intensity distribution near

the boundary of the microdisk from Fig. 4(b) at a circle with $R = 20.1$ μm. As illustrated in the red curve in Fig. 4(c), the field distributes mainly at the position $\varphi = 0, \pi$, which coincides with the result of simulation shaded in blue.

5. CONCLUSION

To conclude, we propose and demonstrate the azimuthally modulated WGMs in a birefringent circular resonator with the assistance of ray dynamics and wave simulations. The integrability of the TE WGMs, experiencing anisotropic refractive index in the azimuthal direction, in circular resonators of X-cut uniaxial crystal is proved by deriving an additional constant besides energy and momentum. On the other hand, directional emission of TE WGMs induced by anisotropic refractive index and its dependence on material dispersion and the resonator's geometrical size are discussed. The anisotropic emission patterns are experimentally acquired with the help of SHG in the X-cut LN microdisks with excellent $\chi^{(2)}$ nonlinearity. This merit possesses excellent potential in the efficient on-chip light communication for its natural directionality since it provides a potential coupling method that bridges the gap between on-chip devices and other free-space optical systems. Moreover, this result is applicable in all kinds of crystalline materials with birefringence, which paves the way for accurate mode control of multi-functional integrated devices.

Disclosures. The authors declare no conflicts of interest.

Data Availability. Data underlying the results presented in this paper are not publicly available at this time but may be obtained from the authors upon reasonable request.

†These authors contributed equally to this work.

REFERENCES

1. K. J. Vahala, "Optical microcavities," Nature **424**, 839–846 (2003).
2. A. Chiasera, Y. Dumeige, P. Feron, M. Ferrari, Y. Jestin, G. N. Conti, S. Pelli, S. Soria, and G. C. Righini, "Spherical whispering-gallery-mode microresonators," Laser Photonics Rev. **4**, 457–482 (2010).
3. L. He, Ş. K. Özdemir, and L. Yang, "Whispering gallery microcavity lasers," Laser Photonics Rev. **7**, 60–82 (2013).
4. M. D. Baaske, M. R. Foreman, and F. Vollmer, "Single-molecule nucleic acid interactions monitored on a label-free microcavity biosensor platform," Nat. Nanotechnol. **9**, 933–939 (2014).
5. C. Wang, M. Zhang, M. Yu, R. Zhu, H. Hu, and M. Loncar, "Monolithic lithium niobate photonic circuits for Kerr frequency comb generation and modulation," Nat. Commun. **10**, 978 (2019).
6. G. Lin and Q. Song, "Review on Kerr frequency comb interaction with Raman, Brillouin, and second order nonlinear effects," Laser Photonics Rev., 2100184 (2021).
7. G. Poberaj, H. Hu, W. Sohler, and P. Guenter, "Lithium niobate on insulator (LNOI) for micro-photonic devices," Laser Photonics Rev. **6**, 488–503 (2012).
8. Q. Song, "Emerging opportunities for ultra-high Q whispering gallery mode microcavities," Sci. China: Phys. Mech. Astron. **62**, 074231 (2019).
9. L. Wang, C. Wang, J. Wang, F. Bo, M. Zhang, Q. Gong, M. Lončar, and Y.-F. Xiao, "High-Q chaotic lithium niobate microdisk cavity," Opt. Lett. **43**, 2917–2920 (2018).
10. Z. Hao, L. Zhang, A. Gao, W. Mao, X. Lyu, X. Gao, F. Bo, F. Gao, G. Zhang, and J. Xu, "Periodically poled lithium niobate whispering gallery mode microcavities on a chip," Sci. China Phys. Mech. Astron. **61**, 114211 (2018).
11. Z. Fang, S. Haque, S. Farajollahi, H. Luo, J. Lin, R. Wu, J. Zhang, Z. Wang, M. Wang, Y. Cheng, and L. Tao, "Polygon coherent modes in a weakly perturbed whispering gallery microresonator for efficient second harmonic, optomechanical, and frequency comb generations," Phys. Rev. Lett. **125**, 173901 (2020).
12. J.-Y. Chen, Z.-H. Ma, Y. M. Sua, Z. Li, C. Tang, and Y.-P. Huang, "Ultra-efficient frequency conversion in quasi-phase-matched lithium niobate microrings," Optica **6**, 1244–1245 (2019).
13. C. Wang, M. Zhang, X. Chen, M. Bertrand, A. Shams-Ansari, S. Chandrasekhar, P. Winzer, and M. Lončar, "Integrated lithium niobate electro-optic modulators operating at CMOS-compatible voltages," Nature **562**, 101–104 (2018).
14. M. He, M. Xu, Y. Ren, J. Jian, Z. Ruan, Y. Xu, S. Gao, S. Sun, X. Wen, L. Zhou, L. Liu, C. Guo, H. Chen, S. Yu, L. Liu, and X. Cai, "High-performance hybrid silicon and lithium niobate Mach–Zehnder modulators for 100 Gbit s⁻¹ and beyond," Nat. Photonics **13**, 359–364 (2019).
15. B. Desiatov, A. Shams-Ansari, M. Zhang, C. Wang, and M. Lončar, "Ultra-low-loss integrated visible photonics using thin-film lithium niobate," Optica **6**, 380–384 (2019).
16. A. Rahim, A. Hermans, B. Wohlfeil, D. Petousi, B. Kuyken, D. Van Thourhout, and R. Baets, "Taking silicon photonics modulators to a higher performance level: state-of-the-art and a review of new technologies," Adv. Photonics **3**, 024003 (2021).
17. C. Wang, C. Langrock, A. Marandi, M. Jankowski, M. Zhang, B. Desiatov, M. M. Fejer, and M. Lončar, "Ultrahigh-efficiency wavelength conversion in nanophotonic periodically poled lithium niobate waveguides," Optica **5**, 1438–1441 (2018).
18. J. Lin, N. Yao, Z. Hao, J. Zhang, W. Mao, M. Wang, W. Chu, R. Wu, Z. Fang, L. Qiao, W. Fang, F. Bo, and Y. Cheng, "Broadband quasi-phase-matched harmonic generation in an on-chip monocrystalline lithium niobate microdisk resonator," Phys. Rev. Lett. **122**, 173903 (2019).
19. Y. He, H. Liang, R. Luo, M. Li, and Q. Lin, "Dispersion engineered high quality lithium niobate microring resonators," Opt. Express **26**, 16315–16322 (2018).
20. J. U. Nöckel and A. D. Stone, "Ray and wave chaos in asymmetric resonant optical cavities," Nature **385**, 45–47 (1997).
21. B. Peng, Ş. K. Özdemir, M. Liertzer, W. Chen, J. Kramer, H. Yılmaz, J. Wiersig, S. Rotter, and L. Yang, "Chiral modes and directional lasing at exceptional points," Proc. Natl. Acad. Sci. USA **113**, 6845–6850 (2016).
22. X. Jiang, L. Shao, S.-X. Zhang, X. Yi, J. Wiersig, L. Wang, Q. Gong, M. Lončar, L. Yang, and Y.-F. Xiao, "Chaos-assisted broadband momentum transformation in optical microresonators," Science **358**, 344–347 (2017).
23. S.-J. Park, J.-H. Lim, Y.-H. Lee, I. Kim, J. Cho, S. Rim, and M. Choi, "Birefringent whispering gallery cavities designed by linear transformation optics," Opt. Express **29**, 9242–9251 (2021).
24. X.-F. Jiang, C.-L. Zou, L. Wang, Q. Gong, and Y.-F. Xiao, "Whispering-gallery microcavities with unidirectional laser emission," Laser Photonics Rev. **10**, 40–61 (2016).
25. S. C. Creagh, H. B. Hamdin, and G. Tanner, "In–out decomposition of boundary integral equations," J. Phys. A **46**, 435203 (2013).
26. H. Cao and J. Wiersig, "Dielectric microcavities: model systems for wave chaos and non-Hermitian physics," Rev. Mod. Phys. **87**, 61–111 (2015).
27. R. W. Boyd, Nonlinear Optics (Academic, 2020).
28. M. Hentschel, H. Schomerus, and R. Schubert, "Husimi functions at dielectric interfaces: inside-outside duality for optical systems and beyond," Europhys. Lett. **62**, 636–642 (2003).

29. Y. Kim, S.-Y. Lee, J.-W. Ryu, I. Kim, J.-H. Han, H.-S. Tae, M. Choi, and B. Min, "Designing whispering gallery modes via transformation optics," Nat. Photonics **10**, 647–652 (2016).

30. I. Kim, J. Cho, Y. Kim, B. Min, J.-W. Ryu, S. Rim, and M. Choi, "Husimi functions at gradient index cavities designed by conformal transformation optics," Opt. Express **26**, 6851–6859 (2018).

31. L. Xu and H. Chen, "Conformal transformation optics," Nat. Photonics **9**, 15–23 (2015).

32. Y.-J. Qian, Q.-T. Cao, S. Wan, Y.-Z. Gu, L.-K. Chen, C.-H. Dong, Q. Song, Q. Gong, and Y.-F. Xiao, "Observation of a manifold in the chaotic phase space of an asymmetric optical microcavity," Photon. Res. **9**, 364–369 (2021).

33. U. Schlarb and K. Betzler, "Influence of the defect structure on the refractive indices of undoped and Mg-doped lithium niobate," Phys. Rev. B **50**, 751–757 (1994).